

1 **Building a machine learning surrogate model for wildfire activities within a global earth**  
2 **system model**

3 Qing Zhu<sup>1,\*</sup>, Fa Li<sup>1,2</sup>, William J. Riley<sup>1</sup>, Li Xu<sup>3</sup>, Lei Zhao<sup>4</sup>, Kunxiaoqia Yuan<sup>1,2</sup>, Huayi Wu<sup>2</sup>,  
4 Jianya Gong<sup>5</sup>, James Randerson<sup>3</sup>

5  
6 <sup>1</sup> Climate and Ecosystem Sciences Division, Climate Sciences Department, Lawrence Berkeley  
7 National Laboratory, Berkeley, CA, USA

8 <sup>2</sup> State Key Laboratory of Information Engineering in Surveying, Mapping and Remote Sensing,  
9 Wuhan University, Wuhan, China

10 <sup>3</sup> Department of Earth System Science, University of California Irvine, Irvine, CA, USA

11 <sup>4</sup> Department of Civil and Environmental Engineering, University of Illinois Urbana-Champaign,  
12 Champaign, IL, USA

13 <sup>5</sup> School of Remote Sensing and Information Engineering, Wuhan University, Wuhan, China

14 \*Correspondence to Qing Zhu (qzhu@lbl.gov)

15 **Abstract**

16 Wildfire is an important ecosystem process, influencing land biogeophysical and  
17 biogeochemical dynamics and atmospheric composition. Fire-driven loss of vegetation cover, for  
18 example, directly modifies the surface energy budget as a consequence of changing albedo,  
19 surface roughness, and partitioning of sensible and latent heat fluxes. Carbon dioxide and  
20 methane emitted by fires contribute to a positive atmospheric forcing, whereas emissions of  
21 carbonaceous aerosols may contribute to surface cooling. Process-based modeling of wildfires in  
22 earth system land models is challenging due to limited understanding of human, climate, and  
23 ecosystem controls on fire number, fire size, and burned area. Integration of mechanistic wildfire  
24 models within Earth system models requires careful parameter calibration, which is  
25 computationally expensive and subject to equifinality. To explore alternative approaches, we  
26 present a deep neural network (DNN) scheme that surrogates the process-based wildfire model  
27 with the Energy Exascale Earth System Model (E3SM) interface. The DNN wildfire model  
28 accurately simulates observed burned area with over 90% higher accuracy with a large reduction  
29 in parameterization time compared with the current process-based wildfire model. The surrogate  
30 wildfire model successfully captured the observed monthly regional burned area during  
31 validation period 2011 to 2015 (coefficient of determination,  $R^2 = 0.93$ ). Since the DNN wildfire  
32 model has the same input and output requirements as the E3SM process-based wildfire model,  
33 our results demonstrate the applicability of machine learning for high accuracy and efficient  
34 large-scale land model development and predictions.

## 35 **1. Introduction**

36 Wildfires burn ~500 million hectares of vegetated land surface each year, which  
37 significantly modifies the physical properties and biogeochemical cycles of terrestrial  
38 ecosystems [Andela *et al.*, 2017; Bond-Lamberty *et al.*, 2007; Pellegrini *et al.*, 2018; Randerson  
39 *et al.*, 2006]. Living vegetation biomass, surface litter, and coarse woody debris are directly  
40 combusted and removed by wildfire [Harden *et al.*, 2006; Walker *et al.*, 2019]. It has been  
41 suggested that global forest would double if fire were eliminated [Bond *et al.*, 2005]. Fire has  
42 multiple important consequences for the climate system, including directly releasing greenhouse  
43 gases (*e.g.*, CO<sub>2</sub>, CH<sub>4</sub>) [Kasischke and Bruhwiler, 2002; Ross *et al.*, 2013] and aerosols [Jiang *et al.*, 2020];  
44 changing land surface albedo and energy budgets [French *et al.*, 2016; Rother and De  
45 Sales, 2020] and land-atmosphere exchanges of heat, mass, and momentum [Chambers and  
46 Chapin, 2002]; limiting plant transpiration and regional water recycling [Brando *et al.*, 2020;  
47 Holden *et al.*, 2018]; and reshaping forest composition [Mekonnen *et al.*, 2019]. In addition,  
48 biomass burning emits a large amount of fine particulate matter that contributes to about 30% of  
49 cloud condensation nuclei globally [Day, 2004]. Soil organic matter decomposition, nitrogen  
50 mineralization, and the richness and diversity of soil fungal communities [Oliver *et al.*, 2015]  
51 could also be influenced by wildfire through modifying litter substrate supply and degraded  
52 enzymatic activities [Bowd *et al.*, 2019; Holden *et al.*, 2018; Pellegrini *et al.*, 2018; Pellegrini *et al.*,  
53 2020].

54 Climate change and land use activities have jointly affected fire spatial distribution,  
55 frequency, and intensity [Andela *et al.*, 2017; Kelley *et al.*, 2019; X Xu *et al.*, 2020] since the pre-  
56 industrial era. For example, warmer and drier climate conditions enhance fuel aridity and favor  
57 fire occurrence in forest ecosystems where fuels have built up over a period of decades and  
58 centuries [Abatzoglou and Williams, 2016; Williams *et al.*, 2019]. Even if annual precipitation  
59 does not decline, redistribution of precipitation towards wet season extreme rainfall events could  
60 contribute to longer dry periods and thus more severe fire activity [X Xu *et al.*, 2020]. Human  
61 activities often shape wildfire activity through regulating patterns of ignition and fire occurrence  
62 (*e.g.*, powerline ignition) [Keeley and Syphard, 2018] and suppressing wildfire activity by means  
63 of land fragmentation, fire management, and livestock grazing [Andela *et al.*, 2017]. In  
64 California, fire density is highly associated with population density and the distance to the  
65 wildland urban interface (WUI) [Syphard *et al.*, 2007]. At the global scale, along gradients of

66 increasing population density, fire frequency initially increases by up to 20% and then gradually  
67 declines in more densely populated areas [Knorr et al., 2014].

68 Although global wildfire burned area has declined over the recent two decades [Andela et  
69 al., 2017], many vulnerable ecosystems and geographic regions have experienced significant  
70 increases in wildfire activity [Abatzoglou and Williams, 2016; Walker et al., 2019] resulting in  
71 large losses of natural resources and economic assets [Papakosta et al., 2017; Stephenson et al.,  
72 2013]. Over western U.S. forests, wildfire has dramatically increased, costing billions of dollars  
73 each year and gaining wide public attention. This regional wildfire increase is mainly driven by  
74 concurrent increases of spring temperature and declining snowpack [Westerling et al., 2006],  
75 mid-summer increases in vapor pressure deficit [Williams et al., 2019], and increases in drought  
76 stress during fall [Goss et al., 2020]. The enhancement of wet and dry oscillations favors initial  
77 vegetation growth and subsequent wildfire activity [Heyerdahl et al., 2002; Saha et al., 2019].

78 Wildfire models have played an important role in many aspects of wildfire research,  
79 including monitoring fire spread [Finney, 1998; Radke et al., 2019], analyzing controllers of  
80 wildfire short-term and long-term variability [Kelley et al., 2019], predicting severity of the  
81 upcoming fire seasons [Preisler and Westerling, 2007] and climate-scale fire variability  
82 [Girardin and Mudelsee, 2008; Yue et al., 2013], and understanding the complex climate-  
83 wildfire-ecosystem feedbacks [Clark et al., 2004; Mekonnen et al., 2019; Zou et al., 2020]. Two  
84 types of wildfire models are widely used: process-based models and data-driven statistical  
85 models [Hantson et al., 2016]. Process-based wildfire models consider detail processes related to  
86 natural fire ignition [Prentice and Mackerras, 1977], anthropogenic ignition [Venevsky et al.,  
87 2002], fire spread and duration [Thonicke et al., 2010], fire suppression [Lenihan and Bachelet,  
88 2015], and fire mass and heat fluxes [F Li et al., 2012]. Process-based wildfire models have been  
89 widely used in dynamic vegetation models and coupled earth system models (ESMs) with  
90 various complexities of parameterization [Fang Li et al., 2019; Rabin et al., 2017]. As more and  
91 more detailed fire processes are considered and parameterized, structural and parametric  
92 uncertainties may increase due to incomplete representation of individual processes and  
93 imperfect mathematical formulation [Riley and Thompson, 2017]. Historically, data-driven  
94 models were often used for fire behavior modeling and aim to track the ignition, spread,  
95 duration, and extinction of individual fires [Finney, 1998; Radke et al., 2019] at fine spatial and  
96 temporal scales. This group of models are more relevant to operational fire research. While

97 process-based wildfire models in the context of global vegetation models or earth system land  
98 models focuses on the gridcell aggregated fire burned area dynamics that are more relevant to  
99 researches on large scale patterns and climate scale predictions [Fang Li et al., 2019; Rabin et  
100 al., 2017]. This study particularly focuses on the second category of wildfire models.

101 Although explicit processes are simulated, the accuracy of process-based wildfire models  
102 are highly dependent on parameterization, which is computationally expensive [Teckentrup et  
103 al., 2018; L Xu et al., 2021; Zhu and Zhuang, 2014]. Data-driven models, however, directly link  
104 the driving variables (e.g., climate factors) to the fire activity using simple statistical models or  
105 more sophisticated machine learning techniques, ignoring the explicit processes and feedbacks  
106 associated with wildfire [Ganapathi Subramanian and Crowley, 2018; Radke et al., 2019; Tonini  
107 et al., 2020]. Through training and validation, statistical representations of wildfire dynamics are  
108 learned by models using principles from machine learning. Data-driven wildfire models are  
109 diverse in terms of driving variables and model structure. For example, many current machine  
110 learning wildfire models rely on remote oceanic dynamics (e.g., sea surface temperature  
111 variability) and atmospheric teleconnections to simulate land surface fire activities [Chen et al.,  
112 2020; Chen et al., 2011; Yu et al., 2020]. Another group of data-driven wildfire models draws  
113 more heavily upon regional climate, plant functional type, and human infrastructure driver  
114 variables [Coffield et al., 2019; Sayad et al., 2019].

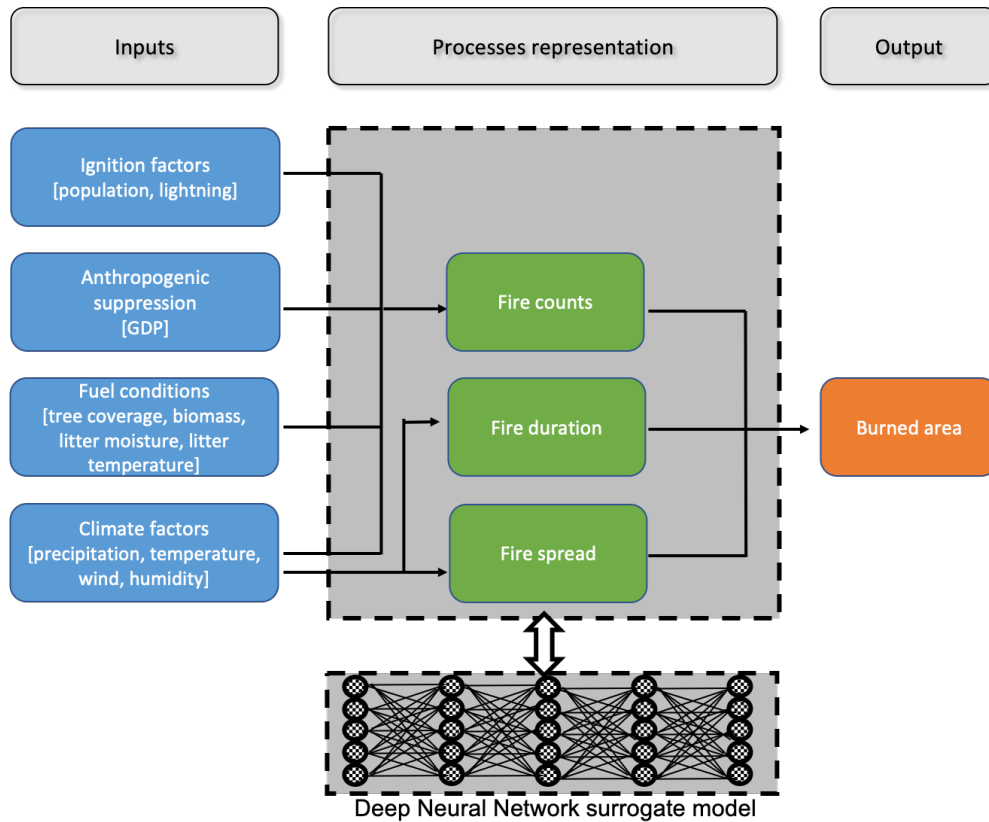
115 In this study, we develop a machine learning wildfire model using the process  
116 representation of wildfire in the Energy Exascale Earth System Model (E3SM) land model  
117 (ELMv1) [Zhu et al., 2019], five observationally inferred burned area products [Andela et al.,  
118 2019; Giglio et al., 2018; Lizundia-Loiola et al., 2020; Lizundia-Loiola et al., 2018; Van Der  
119 Werf et al., 2017], and a deep neural network approach [Goodfellow et al., 2016]. We  
120 implemented a deep learning model that can better capture the complex and non-linear  
121 interactions between controlling factors and wildfire activity. The objectives of this study are to  
122 surrogate the wildfire parameterization in ELMv1 with the deep neural network and improve the  
123 model simulated wildfire burned area across various fire regions [Giglio et al., 2013].

124

## 125 **2. Methodology**

### 126 **2.1 ELMv1 wildfire model**

127           The process-based wildfire model in ELMv1 originates from the Community Land  
128 Model (CLM4.5) [*F Li et al.*, 2012]; we take this wildfire model as the baseline (hereafter refer  
129 to as BASE-Fire) without modification on process representation. BASE-Fire combines  
130 information regarding ignition, fuel conditions, surface climate, and anthropogenic suppression  
131 to simulate total burned area based on the fire counts and spread area of each fire (Figure 1). The  
132 fire count in BASE-Fire is modeled as the sum of anthropogenic ignition and natural ignition,  
133 where the latter is proportional to lightning density [*Prentice and Mackerras*, 1977] and the  
134 former is determined by population density [*Venevsky et al.*, 2002]. Human activity may also  
135 intentionally suppress wildfire occurrence if the fire is detected at early stage. For example,  
136 developed regions with high population density and gross domestic product are less likely to use  
137 fire to remove surface biomass. On the other hand, developed regions more likely suppress fire  
138 given more effective fire management policy and suppression capability. Fire count is also  
139 affected by surface fuel availability (aboveground biomass) and fuel combustibility (relative  
140 humidity, topsoil temperature and moisture). The fire spread area in BASE-Fire is modeled as an  
141 elliptical shaped region controlled by wind speed and fuel wetness [*Rothermel*, 1972] (using  
142 topsoil (0 – 15 cm) moisture as a proxy). The fire duration is set to be one day based on a study  
143 that reported years 2001-2004 mean global fire persistence [*Giglio et al.*, 2006a]. BASE-Fire  
144 also does not explicitly consider roads, rivers, and firefighting activity [*Arora and Boer*, 2005].  
145



146

147 **Figure 1.** Schematic representation of the ELMv1 process-based BASE-Fire model and the  
 148 components to be surrogated with the Deep Neural Network (DNN) model (dark grey).

149

## 150 2.2 Deep neural network wildfire surrogate model

151 We developed the new fire model in two steps: (1) surrogating BASE-Fire with a deep  
 152 neural network (DNN) approach and (2) improving that surrogate model using five  
 153 observationally inferred burned area products (Table S1). First, we surrogated BASE-Fire with a  
 154 DNN approach (hereafter refer to as DNN-Fire) that uses the same input and output variables as  
 155 BASE-Fire but treats the explicit intermediate processes (*e.g.*, ignition, fire spread) as latent  
 156 variables coded by hidden layers in the DNN (Figure 1). DNN-Fire was developed with five  
 157 hidden layers and five neurons in each layer for burned area simulation. The DNN approach uses  
 158 a fully-connected feedforward neural network [*Schmidhuber, 2015*] that comprises input, hidden,  
 159 and output layers:

$$h_1 = f_1(W_1 I + b_1) \quad (1)$$

$$h_2 = f_2(W_2 h_1 + b_2) \quad (2)$$

$$h_3 = f_3(W_3h_2 + b_3) \quad (3)$$

$$h_4 = f_4(W_4h_3 + b_4) \quad (4)$$

$$h_5 = f_5(W_5h_4 + b_5) \quad (5)$$

$$O = f_6(W_6h_5 + b_6) \quad (6)$$

160 where  $I$  denotes the input layer (*e.g.*, climate factors) with 11 neurons, each corresponding to an  
 161 input variable listed in Table 1.  $h_1$ ,  $h_2$ ,  $h_3$ ,  $h_4$ , and  $h_5$  are five hidden vectors that are calculated  
 162 with two steps. First is a linear combination of previous layers' input vector ( $h$ ) and the trainable  
 163 weight parameter matrix [ $W_1$ ,  $W_2$ ,  $W_3$ ,  $W_4$ ,  $W_5$ ,  $W_6$ ], considering biases  $b_1$ ,  $b_2$ ,  $b_3$ ,  $b_4$ ,  $b_5$ , and  $b_6$ .  
 164 Then, nonlinear activation functions  $f_1$ ,  $f_2$ ,  $f_3$ ,  $f_4$ ,  $f_5$ , and  $f_6$ . are applied to the output from the  
 165 previous step. In this study we used *softplus* as the activation function [Zheng *et al.*, 2015] that is  
 166 a non-linear transformation of input signals.  $O$  denotes the output layer that summarize the latent  
 167 variables from the last hidden layer ( $h_5$ ) and calculate burned area.

168 **Table 1.** Input and output variables of ELMv1 BASE-Fire and surrogate DNN-Fire models

Variable category	Variable name	Data source and reference
<i>Input variables</i>		
<b>Fuel conditions</b>	Tree coverage	LUH2 [Hurtt <i>et al.</i> , 2020]
	Fuel load	ELMv1 total biomass [Zhu and Riley, 2015; Zhu <i>et al.</i> , 2019]
	Fuel wetness	ELMv1 topsoil moisture [Zhu and Riley, 2015; Zhu <i>et al.</i> , 2019]
	Fuel temperature	ELMv1 topsoil temperature [Zhu and Riley, 2015; Zhu <i>et al.</i> , 2019]
<b>Climate factors</b>	Precipitation	GSWP3 [Dirmeyer <i>et al.</i> , 2006]
	Near surface temperature	GSWP3 [Dirmeyer <i>et al.</i> , 2006]
	Wind speed	GSWP3 [Dirmeyer <i>et al.</i> , 2006]
	Relative humidity	GSWP3 [Dirmeyer <i>et al.</i> , 2006]
<b>Ignition</b>	Population density	[Dobson <i>et al.</i> , 2000]
	Lightning frequency	NASA-LIS/OTD [Cecil <i>et al.</i> , 2014]
<b>Anthropogenic suppression</b>	GDP	[van Vuuren <i>et al.</i> , 2007]
	Population density	[Dobson <i>et al.</i> , 2000]



<i>output variable</i>	
Burned area	ELMv1 percentage burned area [Zhu and Riley, 2015; Zhu et al., 2019]

169

170           Second, we improved the surrogate DNN-Fire by fine-tuning the weight parameters using  
 171 observations (hereafter refer to DNN-Fire-OBS). Between 2001 and 2010, we initialized  
 172 DNN-Fire-OBS’s weight parameters ( $W_1$ ,  $W_2$ ,  $W_3$ ,  $W_4$ ,  $W_5$ , and  $W_6$ ) using results from DNN-Fire,  
 173 replaced the BASE-Fire burned area by the ensemble mean of five observationally inferred  
 174 burned area products including GFEDv4s [Van Der Werf et al., 2017], Fire\_CCI51 [Lizundia-  
 175 Loiola et al., 2020], Fire\_CCILT11 [Lizundia-Loiola et al., 2018], MODIS MCD64 [Giglio et  
 176 al., 2018], and Fire\_Atlas [Andela et al., 2019] (Table S1), and adjusted weight parameters until  
 177 the model best reproduced the observed burned area. This two-step approach will also allow  
 178 rapid parameterization of the Fire model as new fire data and baseline fire model results become  
 179 available. DNN-Fire-OBS can be more easily generalized since BASE-Fire provides explicit  
 180 physical guidance and a larger-than-observation input and output feature space for development  
 181 of the machine learning fire model. One limitation is the large discrepancy among five burned  
 182 area products. Tuning DNN-Fire towards the ensemble mean of the five products will potentially  
 183 compromise the data difference, however, future work is needed to improve the burned area data  
 184 quality and consistency.

### 185 **2.3 Model setup and simulation protocol**

186           We ran ELMv1 with BASE-Fire at  $1.9^\circ$  by  $2.5^\circ$  spatial resolution [Zhu et al., 2020; Zhu  
 187 et al., 2016] to generate training and testing datasets for the DNN wildfire model. BASE-Fire  
 188 was first spun up for 600 years with accelerated soil decomposition followed by 200 years  
 189 regular spinup with regular soil decomposition [Koven et al., 2013]. The spinup simulations were  
 190 forced with constant atmospheric  $\text{CO}_2$  concentration (285 ppmv) and 1901-1920 repeated  
 191 climate forcing from GSWP3 (Global Soil Wetness Project) [Dirmeyer et al., 2006]. The purpose  
 192 of the spinup was to initialize ecosystem carbon pools and stabilize plant and soil carbon and  
 193 water fluxes. Restarting from the “spunup” conditions, a transient simulation was then conducted  
 194 from 1901 to 2015 with GSWP3 transient climate forcing, atmospheric  $\text{CO}_2$  concentrations, and  
 195 nitrogen and phosphorus deposition [Lamarque et al., 2005; Mahowald et al., 2008]. Wildfire  
 196 associated variables were selected for output with a monthly temporal resolution (Table 1).

197 BASE-Fire output from years 1981 to 2010 were used to train, test, and fine-tune  
 198 DNN-Fire. We developed 14 region-specific models, corresponding to 14 widely used GFED  
 199 regions. For each region, all land gridcells (comprising no fire history, infrequent fire, and  
 200 repeated fire) were concatenated into one data matrix (where rows consist of the number of  
 201 samples and columns of the number of variables). 80% of the data matrix was randomly sampled  
 202 for the training dataset and the remaining 20% of the data were reserved for testing. Furthermore,  
 203 the random sampling was stratified in order to reduce the risk of sampling, e.g., adjacent high  
 204 fire grid cells. All grid cells were first divided into three “strata”: low burn (0-33% percentile),  
 205 median burn (33%-66% percentile), and high burn (67-100% percentile) grid cells based on the  
 206 magnitude of the burn. The stratified random sample assured the sampled grid cells for training  
 207 and testing had the same ratios of low/medium/high burn, thus eliminating the sampling bias  
 208 from spatial autocorrelation [Wang *et al.*, 2012]. In addition to random sampling, we also  
 209 investigated the impacts of data choice on the model performance, by sampling the testing  
 210 datasets within specific years (*e.g.*, 2001-2002, 2003-2004, 2005-2006, 2007-2008, 2009-2010)  
 211 and used the rest of the years for training. We found neglected differences among the models  
 212 (Figure S1) indicating the choice of training/testing data years were not impactful. Therefore, we  
 213 will discuss the results with stratified random sampling approach as the major results throughout  
 214 the paper.

215 All training and testing datasets were normalized to the range [0, 1] with the following  
 216 scaler:

$$X = \frac{X - X_{min}}{X_{max} - X_{min}} \quad (7)$$

217 where  $X$  is the variable vector of interest and  $X_{min}$  and  $X_{max}$  are minimum and maximum values of  
 218  $X$ , respectively. During the training stage, we randomly initialized the weighting parameters (Eq.  
 219 1-6) and optimized them using the Adaptive Moment Estimation method [Kingma and Ba,  
 220 2014], which is a variant of the gradient descent optimization method but considers adaptive  
 221 learning rate and momentum-like exponentially decaying gradients. The parameter optimization  
 222 aimed to minimize a mean squared error cost function:

$$J = \frac{1}{n} \sum_{i=1}^n (y_i^{DNN} - y_i^{BASE})^2 \quad (8)$$

223 where  $y_i^{DNN}$  and  $y_i^{BASE}$  are DNN-Fire and BASE-Fire generated burned area, respectively.  $i$   
 224 represents different gridcell. Cost function  $J$  summarizes the overall magnitude of the error

225 between the surrogate DNN-Fire and BASE-Fire. We then evaluated model performance using  
 226 metrics of mean absolute error (Eqn. 9), Pearson correlation (Eqn. 10), and coefficient of  
 227 determination (Eqn. 11).

$$228 \quad MAE = \frac{1}{n} \sum_{i=1}^n |y_i^{DNN} - y_i^{BASE}| \quad (9)$$

$$229 \quad p = \frac{covariance(y^{DNN}, y^{BASE})}{\sqrt{variance(y^{DNN})variance(y^{BASE})}} \quad (10)$$

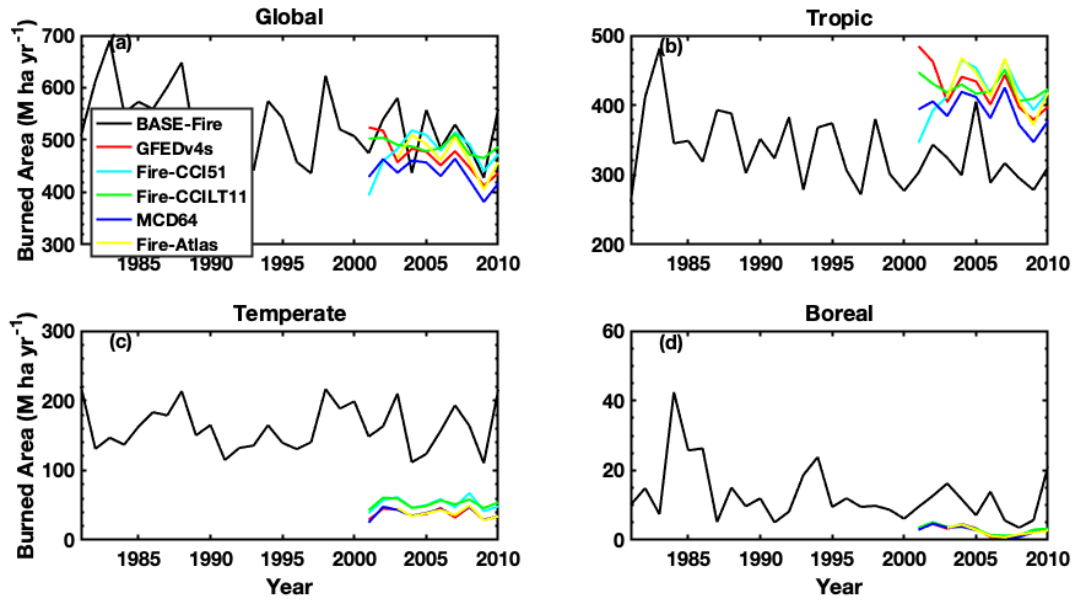
$$230 \quad R^2 = 1 - \frac{\sum_{i=1}^n (y_i^{DNN} - y_i^{BASE})^2}{\sum_{i=1}^n (y_i^{BASE} - y_{mean}^{BASE})^2} \quad (11)$$

231

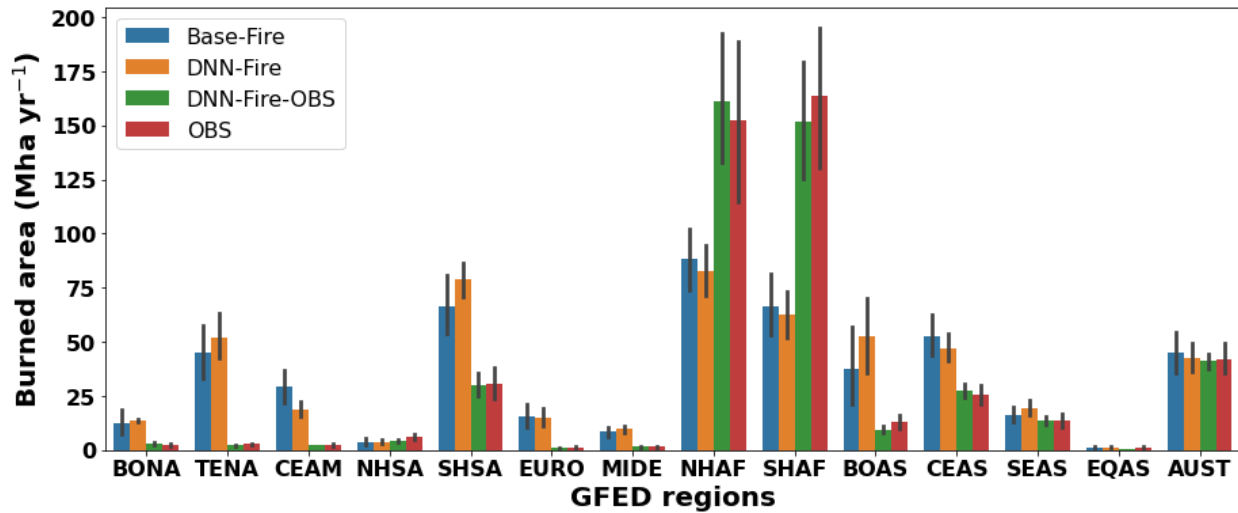
### 232 **3. Results and discussion**

#### 233 **3.1 Evaluation of wildfire surrogate model**

234 BASE-Fire performed reasonably well for total global burned area ( $508 \pm 53$  Mha yr<sup>-1</sup>  
 235 (million hector per year) between years 2001 and 2010 compared with the observational long-  
 236 term average of 424~484 Mha yr<sup>-1</sup>; Figure 2, Table S1). BASE-Fire also captured the global  
 237 declining trend of wildfire burned area over this time period, attributed to a decrease in tropical  
 238 fires [Andela *et al.*, 2017]. At the regional scale, however, BASE-Fire underestimated tropical  
 239 (S23.5° - N23.5°) burned area and overestimated temperate (N23.5° - N67.5°) and boreal (N67.5°  
 240 above) burned area (Figure 2). Large spatial heterogeneity existed for BASE-Fire regional bias.  
 241 For example, over tropical GFED regions, BASE-Fire overestimated wildfire burned area over  
 242 Southern Hemisphere South America (SHSA), but underestimated wildfire burned area over both  
 243 Southern and Northern Hemisphere Africa regions (SHAF and NHAF), despite an overall  
 244 underestimation over the tropical region (Figure 3). In contrast, consistent overestimation  
 245 occurred over all temperate GFED regions. For example, wildfire burned was overestimated by  
 246 about a factor of 16 (~1 versus 16 Mha yr<sup>-1</sup>) over the Europe GFED region (EURO) (Figure 3).  
 247 Although there is room to improve BASE-Fire performance, the parameterization would involve  
 248 large ensemble simulations and computational resources. Instead, we first used BASE-Fire  
 249 generated data as training and testing datasets to parameterize DNN-Fire, then we fine-tuned the  
 250 DNN-Fire model against observed burned area.



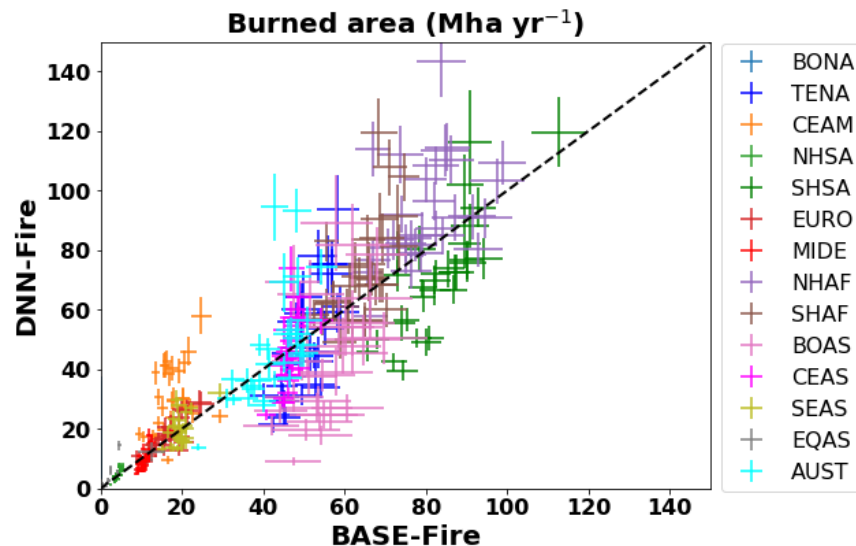
251  
 252 **Figure 2.** ELMv1 process-based model (BASE-Fire) simulated and five observationally inferred  
 253 burned area products (Table S1) at (a) global scale; (b) Tropical (S23.5° -N23.5°); (c) Temperate  
 254 (N23.5° - N 67.5°); and (d) Boreal (north of N 67.5°) regions.  
 255



256  
 257 **Figure 3.** A comparison of wildfire burned area between estimates from the ELMv1 process-  
 258 based model (BASE-Fire), Deep Neural Network wildfire model (DNN-Fire), Deep Neural  
 259 Network wildfire model fine-tuned with observed burned area (DNN-Fire-OBS), and  
 260 observations over 14 GFED fire regions.  
 261

262 Next we parameterized and compared DNN-Fire with BASE-Fire outputs. Using BASE-  
 263 Fire generated  $1.9^\circ \times 2.5^\circ$  resolution datasets of surface fuel conditions (fuel load (vegetation  
 264 biomass), fuel temperature (topsoil temperature), and fuel wetness (topsoil moisture)) with  
 265 gridded climate forcing (GSWP3) [Dirmeyer *et al.*, 2006], land use (LUH2 dataset) [Hurtt *et al.*,  
 266 2020], and social economic [Dobson *et al.*, 2000; van Vuuren *et al.*, 2007] factors, DNN-Fire  
 267 captured the spatial pattern of BASE-fire predicted wildfire activity (Figure 4, Figure S2).  
 268 Across all GFED regions, mean absolute error of DNN-Fire was  $4.4 \text{ Mha yr}^{-1}$  (<1% of total burn  
 269 area), with median and maximum errors of 1.8 and  $13.0 \text{ Mha yr}^{-1}$ , respectively (Figure 3).  
 270 Equatorial Asia (EQAS), Northern Hemisphere South America (NHSA), Central America  
 271 (CEAS), and Europe (EURO) regions had the lowest DNN-Fire errors (<  $1.0 \text{ Mha yr}^{-1}$ ), while  
 272 Southern Hemisphere Africa (SHAF), and Boreal Asia (BOAS) had the largest errors (10-13  
 273  $\text{Mha yr}^{-1}$ ). Overall, the correlation coefficient between BASE-Fire and DNN-Fire simulated  
 274 burned area was 0.91 ( $p$  value < 0.01) and the coefficient of determination ( $R^2$ ) was 0.79. Across  
 275 seasons, DNN-Fire also reasonably captured the BASE-Fire peak fire months (June to October),  
 276 which were dominated by Southern Hemisphere Africa and Southern Hemisphere South  
 277 America (Figure 5).

278 By surrogating BASE-Fire, DNN-Fire is expected to have similar biases and  
 279 uncertainties. The deficiency of BASE-Fire model will propagate to DNN-Fire. In our future  
 280 work we will overcome such limitation by training multiple DNN-Fire models with ensemble  
 281 simulations of BASE-Fire models that differ in critical parameters and vary in model structures.  
 282



283

284 **Figure 4.** The performance of the Deep Neural Network wildfire model (DNN-Fire), compared  
285 with the original ELMv1 process-based wildfire model (BASE-Fire) over 14 GFED regions  
286 between years 2001 and 2010.

287

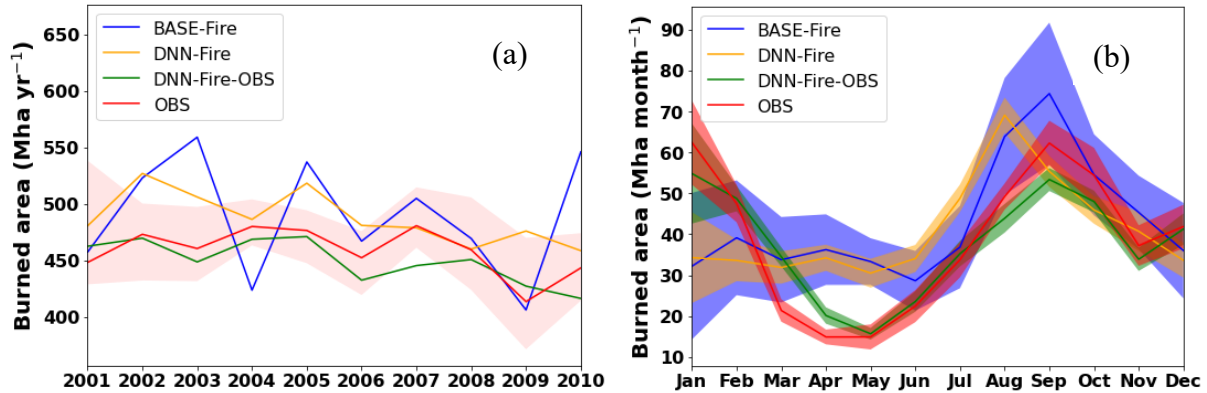
### 288 **3.2 Calibrating the wildfire surrogate model using observations**

289 Although the global pattern was reasonably captured, BASE-Fire had relatively large  
290 biases in several GFED regions, as discussed above. Since DNN-Fire was trained and validated  
291 only with BASE-Fire generated inputs (*e.g.*, fuel conditions) and outputs (burned area), we  
292 expect that, at best, DNN-Fire would have comparable biases as BASE-Fire. Starting from  
293 DNN-Fire, we further calibrated the model weighting parameters to create DNN-Fire-OBS and  
294 validated DNN-Fire-OBS performance using observed burned area from five existing burned  
295 area products (Table S1) between years 2001 and 2010. The calibration time cost several minutes  
296 with Intel Xeon Phi Processor 7250 processor.

297 Dramatic improvements were found in most of the 14 regions simulated by DNN-Fire-  
298 OBS (Figure 3). Overall, DNN-Fire-OBS simulated global long-term average burned area was  
299 458 Mha yr<sup>-1</sup> (compared with observational average 467 Mha yr<sup>-1</sup>). Averaged across 14 regions,  
300 73% reduction of mean absolute error was achieved by DNN-Fire-OBS, compared with the  
301 BASE-Fire model. Pearson correlation coefficient between the DNN-Fire-OBS simulated and  
302 observational burned area was 0.98 (*p* value < 0.001) with an *R*<sup>2</sup> of 0.97. Bias reduction was  
303 disproportionally distributed across the GFED regions (Figure 3). For example, severely burned  
304 regions, including Southern and Northern Hemisphere Africa (SHAF and NHAF) and Southern  
305 Hemisphere South America (SHSA) greatly benefited from the tuning and their regional biases  
306 were reduced by 88, 65, and 51 Mha yr<sup>-1</sup> (or 88%, 89%, 98% reduction), respectively. Although  
307 Temperate Northern America (TENA) and Europe (EURO) wildfire burned area is relatively  
308 small (1-3 Mha yr<sup>-1</sup>), the impacts of wildfire activity were significant due to their high population  
309 densities. DNN-Fire tended to overestimate the burned area in TENA and EURO by 47 and 13  
310 Mha yr<sup>-1</sup>, while DNN-Fire-OBS significantly reduced biases in both regions to less than 0.3 Mha  
311 yr<sup>-1</sup> (a 97-98%% reduction).

312 BASE-Fire tended to overestimate inter-annual variability (IAV) and had opposite burned  
313 area anomalies between years 2001 and 2005. DNN-Fire dampened BASE-Fire's IAV, but had  
314 systematic overestimation of burned area. DNN-Fire-OBS agreed well with the observed IAV

315 between years 2001 and 2010 (Figure 5a). The seasonal cycle was also improved in DNN-Fire-  
 316 OBS in terms of reducing BASE-Fire's overestimation of burned area during peak fire seasons  
 317 (Figure 5b, Figure S3), although we note that DNN-Fire-OBS is biased high during low fire  
 318 seasons (March and April).  
 319



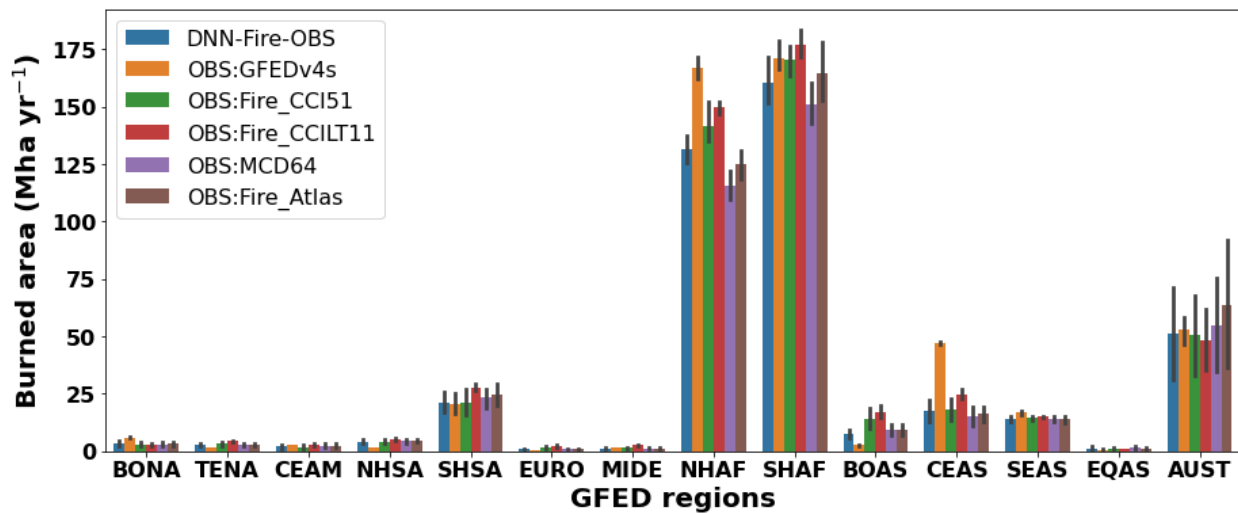
320  
 321 **Figure 5.** Inter-annual variation of burned area from years 2001 to 2010 (a) and the averaged  
 322 seasonal cycle (b) of burned area estimated by the ELMv1 process-based wildfire model (BASE-  
 323 Fire), Deep Neural Network wildfire model (DNN-Fire), Deep Neural Network wildfire model  
 324 fine-tuned with observations (DNN-Fire-OBS), and observations.

325

### 326 3.3 Prognostic simulation and limitations

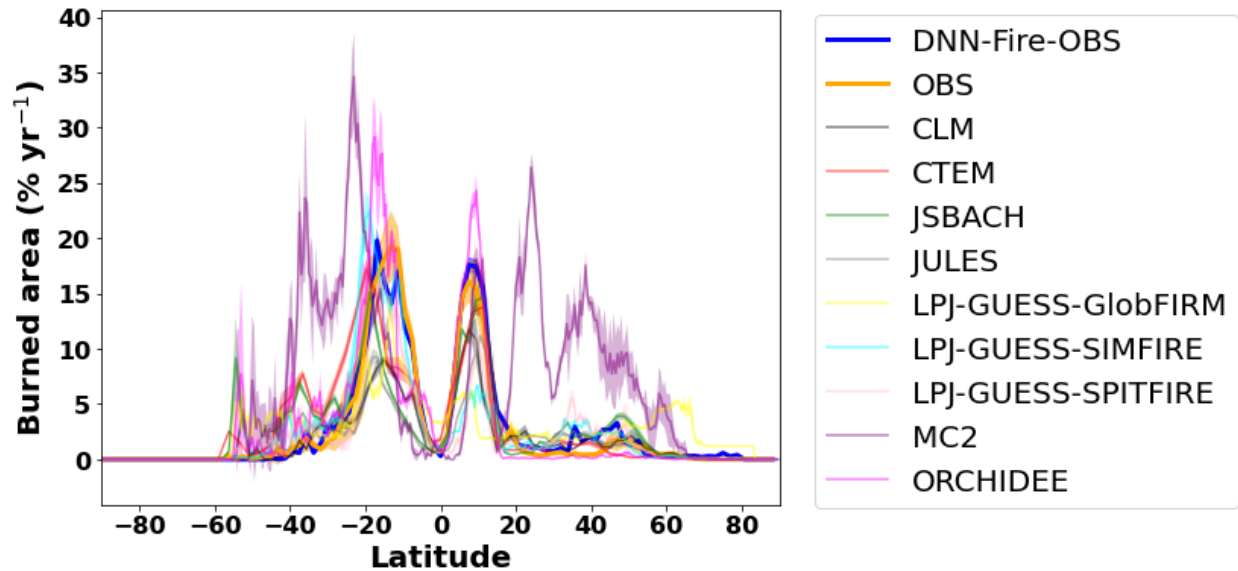
327 We next evaluated the DNN-Fire-OBS model against observations for the period 2011 to  
 328 2015, using data which were not used to train and validate the model. Overall, DNN-Fire-OBS  
 329 simulated 469-514 Mha yr<sup>-1</sup> global burned area, compared with observations 349-509 Mha yr<sup>-1</sup>.  
 330 Note that the large observational ranges were mainly due to the differences among the five  
 331 burned area products rather than the inter-annual variability (Figure 6). Regionally, DNN-Fire-  
 332 OBS overestimated NHAF, SHAF and SHSA annual burned area by 8, 6, 2 Mha yr<sup>-1</sup>,  
 333 respectively (Figure 6) compared with the observational mean. Averaged latitudinal distribution  
 334 of simulated burned area during this period showed that global wildfire activity peaked around  
 335 S10°- S15° and N5°-N10°, together accounting for burning 12-16% of the land surface (Figure  
 336 7). These two peaks were dominated by large burned area over Southern (SHAF) and Northern  
 337 Hemisphere Africa (NHAF) fire regions. Compared with observations, DNN-Fire-OBS  
 338 simulated reasonable burned area latitudinal distributions (Figure 7). We also compared the nine

339 FireMIP models [Rabin *et al.*, 2017; Teckentrup *et al.*, 2018] and found diverse latitudinal  
 340 distribution of burned area. The across model differences were much larger than the inter-annual  
 341 variation simulated by each individual model, which indicated large model structural  
 342 uncertainties. Validation was also conducted for the historical period 1981-2000, when most of  
 343 the satellite based burned area data were not available. Compared with charcoal index inferred  
 344 burned area during 1981-2000 (Figure S4), DNN-Fire-OBS model reasonably captured the  
 345 declining of burned area from  $\sim 530 \text{ Mha yr}^{-1}$  to  $490 \text{ Mha yr}^{-1}$ . In summary, DNN-Fire-OBS  
 346 simulation is reasonably accurate and: (1) improved the simulated wildfire spatial and temporal  
 347 distributions in ELMv1; (2) enabled effective and efficient parameterization of fires at regional  
 348 scale.  
 349



350  
 351 **Figure 6.** Prognostic simulation of annual wildfire burned area with the Deep Neural Network  
 352 wildfire model fine-tuned with observations (DNN-Fire-OBS) compared with five burned area  
 353 products (Table S1) over 2011-2015 for 14 GFED regions.  
 354





355  
 356 **Figure 7.** Prognostic simulation of wildfire burned area (2011-2015) with the Deep Neural  
 357 Network wildfire model fine-tuned with observations (DNN-Fire-OBS) compared with  
 358 observations and nine FireMIP models outputs.

359  
 360 This study focuses on design, development, and parameterization of the DNN fire model  
 361 within the E3SM model interface. In this way the DNN model can be readily coupled in the  
 362 future and iteratively simulate climate, ecosystem fuel conditions, and fire dynamics. Although  
 363 no feedbacks exist between biomass/tree cover and burned area were allowed under current  
 364 offline mode, this study is an important step towards fully coupling E3SM and the DNN-Fire  
 365 models in the future. We acknowledge several challenges and limitations in our modeling  
 366 framework. First, the DNN model uncertainty was subject to the accuracy of climate forcings as  
 367 well as other physical driving variables simulated by the physical wildfire model (ELMv1). For  
 368 example, in this work ELM simulation of soil temperature, soil moisture, fuel load and so on is  
 369 subject to the uncertainty of GSWP3 forcings. Furthermore, those simulated variables served as  
 370 inputs for the DNN model and would result in burned area prediction uncertainty. It was  
 371 challenging to eliminate the forcing uncertainties in this work, but we could at least evaluate the  
 372 magnitude of these uncertainties. We ran the DNN-Fire-OBS model with alternative forcings of  
 373 CRU-JRA, NCEP-DOE2, and CDAS soil moisture from 2001 to 2010 and compared the results  
 374 with DNN-Fire-OBS driven by default inputs (Figure S5). The results showed relatively larger  
 375 uncertainties from climate forcing than that from soil moisture forcing particularly over the

376 major fire regions (e.g., SHSA, SHAF, and NHAF). For fuel load, although no transient dataset  
377 of global living biomass existed yet, we directly compared the ELM model simulated biomass  
378 with the global estimate (GEOCARBON ~ 455 Pg C). We found that the modeled present-day  
379 biomass continuously increased from 425 to 470 Pg C and compared reasonably well with the  
380 global benchmark (Figure S6). Future work will focus on evaluating the uncertainties from dead  
381 fuel load and fuel temperature variables.

382         Second, the original ELMv1 wildfire model has a unified mathematical representation of  
383 how fuel, climate, and social-economic conditions control wildfire burned area [*F Li et al.*,  
384 2012]. However, training one single DNN wildfire model across the globe will produce a model  
385 dominated by gridcells that have high burned area (e.g., Africa). The performance of the trained  
386 DNN model, therefore, will likely have larger biases over the low fire gridcells although the  
387 globally aggregated burned area could be reasonable. We partly overcame this challenge by  
388 applying the widely used 14 GFED fire regions that assume unique and relatively uniform  
389 dynamics over each region [*Giglio et al.*, 2006b], and employed stratified random sampling  
390 method for training and testing datasets. Although the regionally specific wildfire model  
391 introduces additional complexity, it better represents distinct characteristics of wildfire activity  
392 over different climate regimes and biomes [*Zhu and Zhuang*, 2013; *Zou et al.*, 2019] and allows  
393 for future analyses of how the relevant controllers vary across the globe.

394         Thirdly, the cost function and the training of DNN model relied on the normality  
395 assumption of burned area data. Therefore, the DNN model error might be dominated by highly  
396 burned gridcells. A potential solution is to use *log* transformation on non-normal data or the  
397 resultant cost function [*Kelley et al.*, 2021]. Finally, our GFED region-based parameterization  
398 strategy relied on the combination of climate and biome types, while an alternative  
399 parameterization strategy for DNN-Fire model could be based on plant functional type  
400 distributions. Based on our analysis, the PFT-based DNN-Fire model had similar performance  
401 compared with the GFED-based model (Figure S7, S8). Since the GFED regions were defined by  
402 present-day climate and fire regimes, our GFED-based models may not fully capture the changes  
403 of future fire dynamics due to longer-time scale climate and fire regimes changes.

404

#### 405 **4. Conclusions**

406 In this study, we first surrogated the baseline ELMv1 wildfire model with a Deep Neural  
407 Network (DNN) approach (Pearson correlation coefficient = 0.91 ( $p$  value < 0.01),  $R^2 = 0.79$ ).  
408 The development was based on inputs and outputs from the baseline ELMv1 wildfire simulation,  
409 which is process-based and reasonably simulates global burned area, although regional biases  
410 existed. We then calibrated the neural network weights using the years 2001-2010  
411 observationally inferred burned area. The final calibrated DNN wildfire model (DNN-Fire-OBS)  
412 was shown to be more accurate over the 14 GFED regions. For example, reductions in absolute  
413 error over Africa, South America, and Europe were by ~90%. More importantly, the DNN-Fire-  
414 OBS model parameters could be calibrated within minutes, compared with traditional ELMv1  
415 parameterization ensemble simulations that consume a large amount of computational time. The  
416 improved DNN-Fire-OBS model also accurately prognosed global and regional burned area in  
417 the five-year period following the training period from 2011 to 2015 (modeled 469-514 Mha yr<sup>-1</sup>).  
418 We conclude that the improved surrogate wildfire model (DNN-Fire-OBS) developed in this  
419 study can serve as an effective alternative to the process-based fire model currently used in  
420 ELMv1. More broadly, we conclude that machine learning techniques can facilitate earth system  
421 model development, parameterization, and uncertainty reduction with high efficiency and  
422 accuracy.

423

#### 424 **Acknowledgements**

425 This research was supported by Energy Exascale Earth System Modeling (E3SM,  
426 <https://e3sm.org/>) Project and the Reducing Uncertainties in Biogeochemical Interactions  
427 through Synthesis and Computation (RUBISCO) Scientific Focus Area, Office of Biological and  
428 Environmental Research of the U.S. Department of Energy Office of Science. Lawrence  
429 Berkeley National Laboratory (LBNL) is managed by the University of California for the U.S.  
430 Department of Energy under contract DE-AC02-05CH11231.

431

#### 432 **Author contribution**

433 Q.Z., W.J.R, designed the study, Q.Z., W.J.R, L.X., and J.T.R designed model experiments,  
434 Q.Z. and F.L. wrote code and run experiments, L.Z, K.Y, H.W., J.G all contribute to the results  
435 interpretation, and writing.

436

437 **Code availability**

438 <https://zenodo.org/record/5508795#.YUGjg55KiDU>

439

440 **Data availability**

441 GFEDv4s: [https://daac.ornl.gov/VEGETATION/guides/fire\\_emissions\\_v4.html](https://daac.ornl.gov/VEGETATION/guides/fire_emissions_v4.html)

442 Fire\_CCI51: [https://geogra.uah.es/fire\\_cci/firecci51.php](https://geogra.uah.es/fire_cci/firecci51.php)

443 Fire\_CCILT11: [https://geogra.uah.es/fire\\_cci/fireccilt11.php](https://geogra.uah.es/fire_cci/fireccilt11.php)

444 MCD64: [https://modis-fire.umd.edu/files/MODIS\\_C6\\_Fire\\_User\\_Guide\\_C.pdf](https://modis-fire.umd.edu/files/MODIS_C6_Fire_User_Guide_C.pdf)

445 Fire\_Atlas: <https://www.globalfiredata.org/fireatlas.html>

446 FireMIP model outputs: <https://zenodo.org/record/3555562/accessrequest>

447

448 **Reference**

449 Abatzoglou, J. T., and A. P. Williams (2016), Impact of anthropogenic climate change on wildfire  
450 across western US forests, *Proceedings of the National Academy of Sciences*, 113(42), 11770-  
451 11775.

452 Andela, N., D. Morton, L. Giglio, Y. Chen, G. Van Der Werf, P. Kasibhatla, R. DeFries, G. Collatz, S.  
453 Hantson, and S. Kloster (2017), A human-driven decline in global burned area, *Science*,  
454 356(6345), 1356-1362.

455 Andela, N., D. C. Morton, L. Giglio, R. Paugam, Y. Chen, S. Hantson, G. R. Van Der Werf, and J. T.  
456 Randerson (2019), The Global Fire Atlas of individual fire size, duration, speed and direction,  
457 *Earth System Science Data*, 11(2), 529-552.

458 Arora, V. K., and G. J. Boer (2005), Fire as an interactive component of dynamic vegetation  
459 models, *Journal of Geophysical Research: Biogeosciences*, 110(G2).

460 Bond, W. J., F. I. Woodward, and G. F. Midgley (2005), The global distribution of ecosystems in a  
461 world without fire, *New phytologist*, 165(2), 525-538.

462 Bond-Lamberty, B., S. D. Peckham, D. E. Ahl, and S. T. Gower (2007), Fire as the dominant driver  
463 of central Canadian boreal forest carbon balance, *Nature*, 450(7166), 89-92.

464 Bowd, E. J., S. C. Banks, C. L. Strong, and D. B. Lindenmayer (2019), Long-term impacts of  
465 wildfire and logging on forest soils, *Nature Geoscience*, 12(2), 113-118.

466 Brando, P., B. Soares-Filho, L. Rodrigues, A. Assunção, D. Morton, D. Tuchsneider, E.  
467 Fernandes, M. Macedo, U. Oliveira, and M. Coe (2020), The gathering firestorm in southern  
468 Amazonia, *Science advances*, 6(2), eaay1632.

469 Cecil, D. J., D. E. Buechler, and R. J. Blakeslee (2014), Gridded lightning climatology from TRMM-  
470 LIS and OTD: Dataset description, *Atmospheric Research*, 135, 404-414.

471 Chambers, S., and F. Chapin (2002), Fire effects on surface-atmosphere energy exchange in  
472 Alaskan black spruce ecosystems: Implications for feedbacks to regional climate, *Journal of*  
473 *Geophysical Research: Atmospheres*, 107(D1), FFR 1-1-FFR 1-17.

474 Chen, Y., J. T. Randerson, S. R. Coffield, E. Foufoula-Georgiou, P. Smyth, C. A. Graff, D. C.

475 Morton, N. Andela, G. R. van der Werf, and L. Giglio (2020), Forecasting global fire emissions on

476 subseasonal to seasonal (S2S) time scales, *Journal of advances in modeling earth systems*, 12(9),  
477 e2019MS001955.

478 Chen, Y., J. T. Randerson, D. C. Morton, R. S. DeFries, G. J. Collatz, P. S. Kasibhatla, L. Giglio, Y.  
479 Jin, and M. E. Marlier (2011), Forecasting fire season severity in South America using sea  
480 surface temperature anomalies, *Science*, 334(6057), 787-791.

481 Clark, T. L., J. Coen, and D. Latham (2004), Description of a coupled atmosphere–fire model,  
482 *International Journal of Wildland Fire*, 13(1), 49-63.

483 Coffield, S. R., C. A. Graff, Y. Chen, P. Smyth, E. Foufoula-Georgiou, and J. T. Randerson (2019),  
484 Machine learning to predict final fire size at the time of ignition, *International journal of*  
485 *wildland fire*.

486 Day, C. (2004), Smoke from burning vegetation changes the coverage and behavior of clouds,  
487 *PhT*, 57(5), 24-24.

488 Dirmeyer, P. A., X. Gao, M. Zhao, Z. Guo, T. Oki, and N. Hanasaki (2006), GSWP-2: Multimodel  
489 analysis and implications for our perception of the land surface, *Bulletin of the American*  
490 *Meteorological Society*, 87(10), 1381-1398.

491 Dobson, J. E., E. A. Bright, P. R. Coleman, R. C. Durfee, and B. A. Worley (2000), LandScan: a  
492 global population database for estimating populations at risk, *Photogrammetric engineering*  
493 *and remote sensing*, 66(7), 849-857.

494 Finney, M. A. (1998), *FARSITE, Fire Area Simulator--model development and evaluation*, US  
495 Department of Agriculture, Forest Service, Rocky Mountain Research Station.

496 French, N. H., M. A. Whitley, and L. K. Jenkins (2016), Fire disturbance effects on land surface  
497 albedo in Alaskan tundra, *Journal of Geophysical Research: Biogeosciences*, 121(3), 841-854.

498 Ganapathi Subramanian, S., and M. Crowley (2018), Using spatial reinforcement learning to  
499 build forest wildfire dynamics models from satellite images, *Frontiers in ICT*, 5, 6.

500 Giglio, L., L. Boschetti, D. P. Roy, M. L. Humber, and C. O. Justice (2018), The Collection 6 MODIS  
501 burned area mapping algorithm and product, *Remote sensing of environment*, 217, 72-85.

502 Giglio, L., I. Csiszar, and C. O. Justice (2006a), Global distribution and seasonality of active fires  
503 as observed with the Terra and Aqua Moderate Resolution Imaging Spectroradiometer (MODIS)  
504 sensors, *Journal of geophysical research: Biogeosciences*, 111(G2).

505 Giglio, L., J. T. Randerson, and G. R. Van Der Werf (2013), Analysis of daily, monthly, and annual  
506 burned area using the fourth-generation global fire emissions database (GFED4), *Journal of*  
507 *Geophysical Research: Biogeosciences*, 118(1), 317-328.

508 Giglio, L., G. Van der Werf, J. Randerson, G. Collatz, and P. Kasibhatla (2006b), Global estimation  
509 of burned area using MODIS active fire observations.

510 Girardin, M. P., and M. Mudelsee (2008), Past and future changes in Canadian boreal wildfire  
511 activity, *Ecological Applications*, 18(2), 391-406.

512 Goodfellow, I., Y. Bengio, and A. Courville (2016), *Deep learning*, MIT press Cambridge.

513 Goss, M., D. L. Swain, J. T. Abatzoglou, A. Sarhadi, C. A. Kolden, A. P. Williams, and N. S.  
514 Diffenbaugh (2020), Climate change is increasing the likelihood of extreme autumn wildfire  
515 conditions across California, *Environmental Research Letters*, 15(9), 094016.

516 Hantson, S., A. Arneeth, S. P. Harrison, D. I. Kelley, I. C. Prentice, S. S. Rabin, and S. Archibald  
517 (2016), The status and challenge of global fire modelling, *Biogeosciences*, 13, 3359-3375.

518 Harden, J. W., K. L. Manies, M. R. Turetsky, and J. C. Neff (2006), Effects of wildfire and  
519 permafrost on soil organic matter and soil climate in interior Alaska, *Global Change Biology*,  
520 12(12), 2391-2403.

521 Heyerdahl, E. K., L. B. Brubaker, and J. K. Agee (2002), Annual and decadal climate forcing of  
522 historical fire regimes in the interior Pacific Northwest, USA, *The Holocene*, 12(5), 597-604.

523 Holden, Z. A., A. Swanson, C. H. Luce, W. M. Jolly, M. Maneta, J. W. Oyler, D. A. Warren, R.  
524 Parsons, and D. Affleck (2018), Decreasing fire season precipitation increased recent western  
525 US forest wildfire activity, *Proceedings of the National Academy of Sciences*, 115(36), E8349-  
526 E8357.

527 Hurtt, G. C., L. Chini, R. Sahajpal, S. Frolking, B. L. Boudirsky, K. Calvin, J. C. Doelman, J. Fisk, S.  
528 Fujimori, and K. K. Goldewijk (2020), Harmonization of global land-use change and management  
529 for the period 850–2100 (LUH2) for CMIP6, *Geoscientific Model Development Discussions*, 1-65.

530 Jiang, Y., X.-Q. Yang, X. Liu, Y. Qian, K. Zhang, M. Wang, F. Li, Y. Wang, and Z. Lu (2020), Impacts  
531 of wildfire aerosols on global energy budget and climate: The role of climate feedbacks, *Journal*  
532 *of Climate*, 33(8), 3351-3366.

533 Kasischke, E. S., and L. P. Bruhwiler (2002), Emissions of carbon dioxide, carbon monoxide, and  
534 methane from boreal forest fires in 1998, *Journal of Geophysical Research: Atmospheres*,  
535 107(D1), FFR 2-1-FFR 2-14.

536 Keeley, J. E., and A. D. Slyphard (2018), Historical patterns of wildfire ignition sources in  
537 California ecosystems, *International journal of wildland fire*, 27(12), 781-799.

538 Kelley, D. I., I. Bistinas, R. Whitley, C. Burton, T. R. Marthews, and N. Dong (2019), How  
539 contemporary bioclimatic and human controls change global fire regimes, *Nature Climate*  
540 *Change*, 9(9), 690-696.

541 Kelley, D. I., B. Chantelle, H. Chris, M. A. Brown, W. Rhys, and D. Ning (2021), Low  
542 meteorological influence found in 2019 Amazonia fires, *Biogeosciences*, 18, 787-804.

543 Kingma, D. P., and J. Ba (2014), Adam: A method for stochastic optimization, *arXiv preprint*  
544 *arXiv:1412.6980*.

545 Knorr, W., T. Kaminski, A. Arneth, and U. Weber (2014), Impact of human population density on  
546 fire frequency at the global scale, *Biogeosciences*, 11(4), 1085-1102.

547 Koven, C. D., W. J. Riley, Z. M. Subin, J. Y. Tang, M. S. Torn, W. D. Collins, G. B. Bonan, D. M.  
548 Lawrence, and S. C. Swenson (2013), The effect of vertically resolved soil biogeochemistry and  
549 alternate soil C and N models on C dynamics of CLM4, *Biogeosciences*, 10, 7109-7131.

550 Lamarque, J. F., J. T. Kiehl, G. P. Brasseur, T. Butler, P. Cameron-Smith, W. D. Collins, W. J.  
551 Collins, C. Granier, D. Hauglustaine, and P. G. Hess (2005), Assessing future nitrogen deposition  
552 and carbon cycle feedback using a multimodel approach: Analysis of nitrogen deposition,  
553 *Journal of Geophysical Research: Atmospheres*, 110(D19).

554 Lenihan, J. M., and D. Bachelet (2015), Historical climate and suppression effects on simulated  
555 fire and carbon dynamics in the conterminous United States, *Global Vegetation Dynamics:  
556 Concepts and Applications in the MC1 Model*, edited by: Bachelet, D. and Turner, D., *AGU*  
557 *Geophysical Monographs*, 214, 17-30.

558 Li, F., M. Val Martin, M. O. Andreae, A. Arneth, S. Hantson, J. W. Kaiser, G. Lasslop, C. Yue, D.  
559 Bachelet, and M. Forrest (2019), Historical (1700–2012) global multi-model estimates of the fire  
560 emissions from the Fire Modeling Intercomparison Project (FireMIP), *Atmospheric Chemistry*  
561 *and Physics*, 19(19), 12545-12567.

562 Li, F., X. Zeng, and S. Levis (2012), A process-based fire parameterization of intermediate  
563 complexity in a Dynamic Global Vegetation Model, *Biogeosciences*, 9(7).

564 Lizundia-Loiola, J., G. Otón, R. Ramo, and E. Chuvieco (2020), A spatio-temporal active-fire  
565 clustering approach for global burned area mapping at 250 m from MODIS data, *Remote*  
566 *Sensing of Environment*, 236, 111493.

567 Lizundia-Loiola, J., M. Pettinari, E. Chuvieco, T. Storm, and J. Gómez-Dans (2018), ESA CCI ECV  
568 Fire Disturbance: Algorithm Theoretical Basis Document-MODIS, version 2.0, edited,  
569 Fire\_cci\_D2.

570 Mahowald, N., T. D. Jickells, A. R. Baker, P. Artaxo, C. R. Benitez-Nelson, G. Bergametti, T. C.  
571 Bond, Y. Chen, D. D. Cohen, and B. Herut (2008), Global distribution of atmospheric phosphorus  
572 sources, concentrations and deposition rates, and anthropogenic impacts, *Global*  
573 *Biogeochemical Cycles*, 22(4).

574 Mekonnen, Z. A., W. J. Riley, J. T. Randerson, R. F. Grant, and B. M. Rogers (2019), Expansion of  
575 high-latitude deciduous forests driven by interactions between climate warming and fire,  
576 *Nature plants*, 5(9), 952-958.

577 Oliver, A. K., M. A. Callahan Jr, and A. Jumpponen (2015), Soil fungal communities respond  
578 compositionally to recurring frequent prescribed burning in a managed southeastern US forest  
579 ecosystem, *Forest Ecology and Management*, 345, 1-9.

580 Papakosta, P., G. Xanthopoulos, and D. Straub (2017), Probabilistic prediction of wildfire  
581 economic losses to housing in Cyprus using Bayesian network analysis, *International journal of*  
582 *wildland fire*, 26(1), 10-23.

583 Pellegrini, A. F., A. Ahlström, S. E. Hobbie, P. B. Reich, L. P. Nieradzik, A. C. Staver, B. C.  
584 Scharenbroch, A. Jumpponen, W. R. Anderegg, and J. T. Randerson (2018), Fire frequency drives  
585 decadal changes in soil carbon and nitrogen and ecosystem productivity, *Nature*, 553(7687),  
586 194-198.

587 Pellegrini, A. F., S. E. Hobbie, P. B. Reich, A. Jumpponen, E. J. Brookshire, A. C. Caprio, C.  
588 Coetsee, and R. B. Jackson (2020), Repeated fire shifts carbon and nitrogen cycling by changing  
589 plant inputs and soil decomposition across ecosystems, *Ecological Monographs*, e01409.

590 Preisler, H. K., and A. L. Westerling (2007), Statistical model for forecasting monthly large  
591 wildfire events in western United States, *Journal of Applied Meteorology and Climatology*,  
592 46(7), 1020-1030.

593 Prentice, S., and D. Mackerras (1977), The ratio of cloud to cloud-ground lightning flashes in  
594 thunderstorms, *Journal of Applied Meteorology*, 16(5), 545-550.

595 Rabin, S. S., J. R. Melton, G. Lasslop, D. Bachelet, M. Forrest, S. Hantson, J. O. Kaplan, F. Li, S.  
596 Mangeon, and D. S. Ward (2017), The Fire Modeling Intercomparison Project (FireMIP), phase  
597 1: experimental and analytical protocols with detailed model descriptions, *Geoscientific Model*  
598 *Development*, 10(3), 1175-1197.

599 Radke, D., A. Hessler, and D. Ellsworth (2019), FireCast: Leveraging Deep Learning to Predict  
600 Wildfire Spread, paper presented at IJCAI.

601 Randerson, J. T., H. Liu, M. G. Flanner, S. D. Chambers, Y. Jin, P. G. Hess, G. Pfister, M. Mack, K.  
602 Treseder, and L. Welp (2006), The impact of boreal forest fire on climate warming, *science*,  
603 314(5802), 1130-1132.

604 Riley, K., and M. Thompson (2017), An uncertainty analysis of wildfire modeling, *Natural hazard*  
605 *uncertainty assessment: modeling and decision support. Monograph*, 223, 193-213.

606 Ross, A. N., M. J. Wooster, H. Boesch, and R. Parker (2013), First satellite measurements of  
607 carbon dioxide and methane emission ratios in wildfire plumes, *Geophysical Research Letters*,  
608 40(15), 4098-4102.

609 Rother, D., and F. De Sales (2020), Impact of Wildfire on the Surface Energy Balance in Six  
610 California Case Studies, *Boundary-Layer Meteorology*, 1-24.

611 Rothermel, R. C. (1972), A mathematical model for predicting fire spread in wildland fuels,  
612 *Intermountain Forest & Range Experiment Station, Forest Service, US Department of*  
613 *Agriculture*, 115.

614 Saha, M. V., T. M. Scanlon, and P. D'Odorico (2019), Climate seasonality as an essential  
615 predictor of global fire activity, *Global Ecology and Biogeography*, 28(2), 198-210.

616 Sayad, Y. O., H. Mousannif, and H. Al Moatassime (2019), Predictive modeling of wildfires: A  
617 new dataset and machine learning approach, *Fire safety journal*, 104, 130-146.

618 Schmidhuber, J. (2015), Deep learning in neural networks: An overview, *Neural networks*, 61,  
619 85-117.

620 Stephenson, C., J. Handmer, and R. Betts (2013), Estimating the economic, social and  
621 environmental impacts of wildfires in Australia, *Environmental Hazards*, 12(2), 93-111.

622 Syphard, A. D., V. C. Radeloff, J. E. Keeley, T. J. Hawbaker, M. K. Clayton, S. I. Stewart, and R. B.  
623 Hammer (2007), Human influence on California fire regimes, *Ecological applications*, 17(5),  
624 1388-1402.

625 Teckentrup, L., G. Lasslop, D. Bachelet, M. Forrest, S. Hantson, F. Li, J. R. Melton, C. Yue, A.  
626 Arneeth, and S. P. Harrison (2018), Simulations of historical burned area: A comparison of global  
627 fire models in FireMIP, *EGUGA*, 17537.

628 Thonicke, K., A. Spessa, I. Prentice, S. P. Harrison, L. Dong, and C. Carmona-Moreno (2010), The  
629 influence of vegetation, fire spread and fire behaviour on biomass burning and trace gas  
630 emissions: results from a process-based model, *Biogeosciences*, 7(6), 1991-2011.

631 Tonini, M., M. D'Andrea, G. Biondi, S. Degli Esposti, A. Trucchia, and P. Fiorucci (2020), A  
632 Machine Learning-Based Approach for Wildfire Susceptibility Mapping. The Case Study of the  
633 Liguria Region in Italy, *Geosciences*, 10(3), 105.

634 Van Der Werf, G. R., J. T. Randerson, L. Giglio, T. T. Van Leeuwen, Y. Chen, B. M. Rogers, M. Mu,  
635 M. J. Van Marle, D. C. Morton, and G. J. Collatz (2017), Global fire emissions estimates during  
636 1997-2016, *Earth System Science Data*, 9(2), 697-720.

637 van Vuuren, D. P., P. L. Lucas, and H. Hilderink (2007), Downscaling drivers of global  
638 environmental change: Enabling use of global SRES scenarios at the national and grid levels,  
639 *Global environmental change*, 17(1), 114-130.

640 Venevsky, S., K. Thonicke, S. Sitch, and W. Cramer (2002), Simulating fire regimes in human-  
641 dominated ecosystems: Iberian Peninsula case study, *Global Change Biology*, 8(10), 984-998.

642 Walker, X. J., J. L. Baltzer, S. G. Cumming, N. J. Day, C. Ebert, S. Goetz, J. F. Johnstone, S. Potter,  
643 B. M. Rogers, and E. A. Schuur (2019), Increasing wildfires threaten historic carbon sink of  
644 boreal forest soils, *Nature*, 572(7770), 520-523.

645 Wang, J.-F., A. Stein, B.-B. Gao, and Y. Ge (2012), A review of spatial sampling, *Spatial Statistics*,  
646 2, 1-14.

647 Westerling, A. L., H. G. Hidalgo, D. R. Cayan, and T. W. Swetnam (2006), Warming and earlier  
648 spring increase western US forest wildfire activity, *science*, 313(5789), 940-943.



649 Williams, A. P., J. T. Abatzoglou, A. Gershunov, J. Guzman-Morales, D. A. Bishop, J. K. Balch, and  
650 D. P. Lettenmaier (2019), Observed impacts of anthropogenic climate change on wildfire in  
651 California, *Earth's Future*, 7(8), 892-910.

652 Xu, L., Z. Qing, J. R. William, C. Yang, W. Hailong, M. Po-Lun, and T. R. James (2021), The  
653 influence of fire aerosols on surface climate and gross primary production in the Energy  
654 Exascale Earth System Model (E3SM), *Journal of Climate* 34, 7219-7238.

655 Xu, X., G. Jia, X. Zhang, W. J. Riley, and Y. Xue (2020), Climate regime shift and forest loss  
656 amplify fire in Amazonian forests, *Global Change Biology*, 26(10), 5874-5885.

657 Yu, Y., J. Mao, P. E. Thornton, M. Notaro, S. D. Wullschleger, X. Shi, F. M. Hoffman, and Y. Wang  
658 (2020), Quantifying the drivers and predictability of seasonal changes in African fire, *Nature*  
659 *Communications*, 11(1), 1-8.

660 Yue, X., L. J. Mickley, J. A. Logan, and J. O. Kaplan (2013), Ensemble projections of wildfire  
661 activity and carbonaceous aerosol concentrations over the western United States in the mid-  
662 21st century, *Atmospheric Environment*, 77, 767-780.

663 Zheng, H., Z. Yang, W. Liu, J. Liang, and Y. Li (2015), Improving deep neural networks using  
664 softplus units, paper presented at 2015 International Joint Conference on Neural Networks  
665 (IJCNN), IEEE.

666 Zhu, Q., and W. J. Riley (2015), Improved modelling of soil nitrogen losses, *Nature Climate*  
667 *Change*, 5(8), 705-706.

668 Zhu, Q., W. J. Riley, C. M. Iversen, and J. Kattge (2020), Assessing impacts of plant stoichiometric  
669 traits on terrestrial ecosystem carbon accumulation using the E3SM land model, *Journal of*  
670 *Advances in Modeling Earth Systems*, 12(4), e2019MS001841.

671 Zhu, Q., W. J. Riley, J. Tang, N. Collier, F. M. Hoffman, X. Yang, and G. Bisht (2019), Representing  
672 nitrogen, phosphorus, and carbon interactions in the E3SM Land Model: Development and  
673 global benchmarking, *Journal of Advances in Modeling Earth Systems*, doi:  
674 10.1029/2018MS001571.

675 Zhu, Q., W. J. Riley, J. Tang, and C. D. Koven (2016), Multiple soil nutrient competition between  
676 plants, microbes, and mineral surfaces: model development, parameterization, and example  
677 applications in several tropical forests, *Biogeosciences*, 13, 341-363, doi:10.5194/bgd-12-4057-  
678 2015.

679 Zhu, Q., and Q. Zhuang (2013), Improving the quantification of terrestrial ecosystem carbon  
680 dynamics over the United States using an adjoint method, *Ecosphere*, 4(10), doi:  
681 dx.doi.org/10.1890/ES1813-00058.00051.

682 Zhu, Q., and Q. Zhuang (2014), Parameterization and sensitivity analysis of a process-based  
683 terrestrial ecosystem model using adjoint method, *Journal of Advances in Modeling Earth*  
684 *Systems*, 6(2), 315-331.

685 Zou, Y., Y. Wang, Z. Ke, H. Tian, J. Yang, and Y. Liu (2019), Development of a REgion-specific  
686 ecosystem feedback fire (RESFire) model in the Community Earth System Model, *Journal of*  
687 *Advances in Modeling Earth Systems*, 11(2), 417-445.

688 Zou, Y., Y. Wang, Y. Qian, H. Tian, J. Yang, and E. Alvarado (2020), Using CESM-RESFire to  
689 understand climate-fire-ecosystem interactions and the implications for decadal climate  
690 variability, *Atmospheric Chemistry and Physics*, 20(PNNL-SA-150222).

691

692 **Supplementary Material**

693

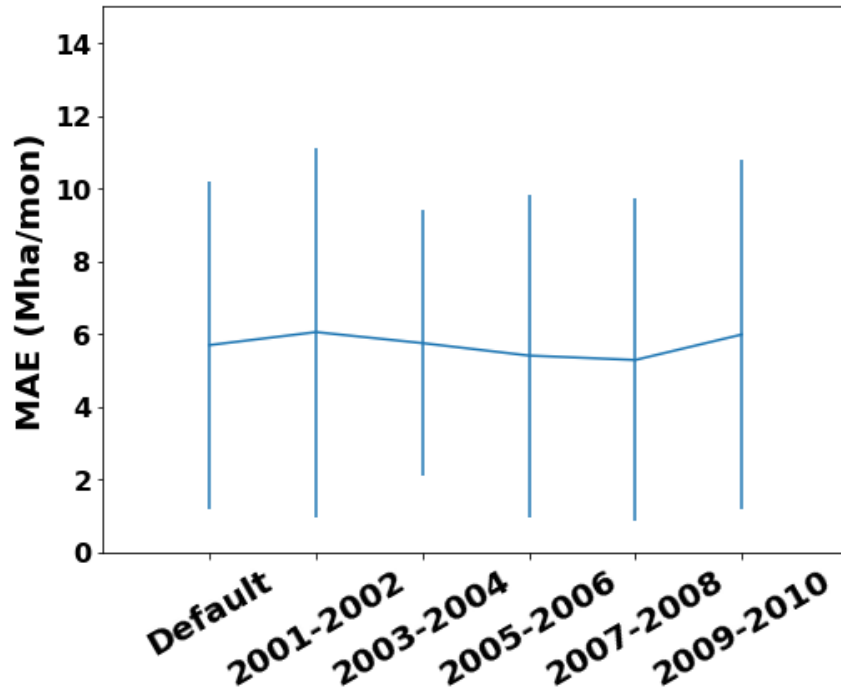
694 Table S1. Burned area datasets used in this study

695

Dataset name	Temporal range	Spatial resolution	Burned area, mean (std)	Citations
GFEDv4s	1997-2015	0.25 degree	455(39)	(Van Der Werf, Randerson et al. 2017)
Fire_CCI51	2001-2019	0.25 degree	476(26)	(Lizundia-Loiola, Otón et al. 2020)
Fire_CCILT11	1982-2018	0.25 degree	484(20)	(Lizundia-Loiola, Pettinari et al. 2018)
MCD64	2001-2019	0.25 degree	424(35)	(Giglio, Boschetti et al. 2018)
Fire_Atlas	2003-2016	0.25x0.25 degree	459(43)	(Andela, Morton et al. 2019)

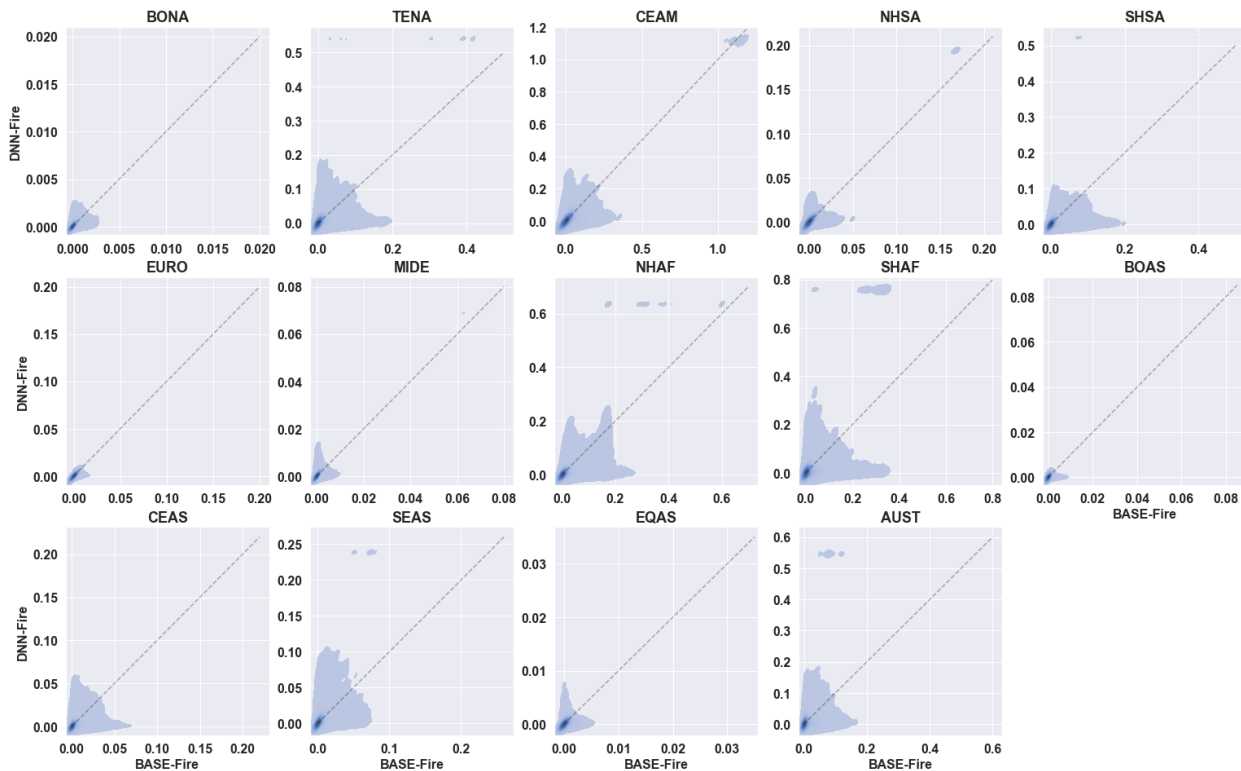
696 **Note:** the long-term average global burned area was calculated using data with the same  
 697 overlapping temporal range (2003-2015), unit Mha yr<sup>-1</sup>

698



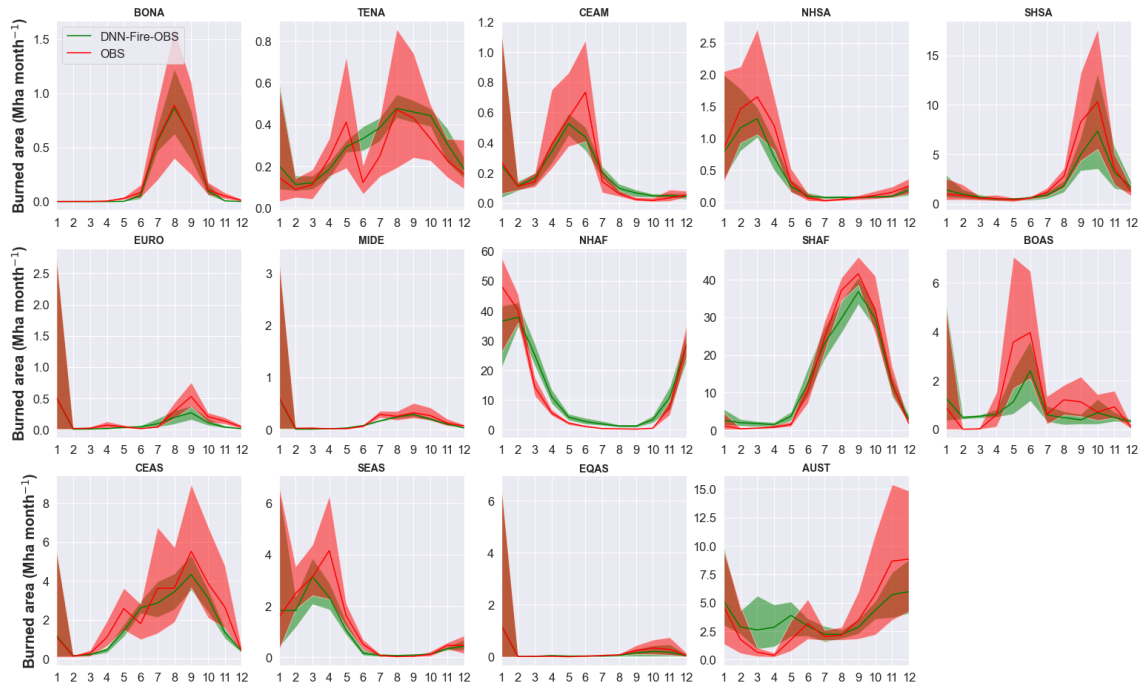
700  
701  
702  
703  
704

**Figure S1.** Model performance evaluated with testing datasets of default (20% randomly selected samples), or fixed to 2001-2002 period, 2003-2004 period, 2005-2006 period, 2007-2008 period, and 2009-2010 periods (the rest of the dataset was used as a training dataset.).

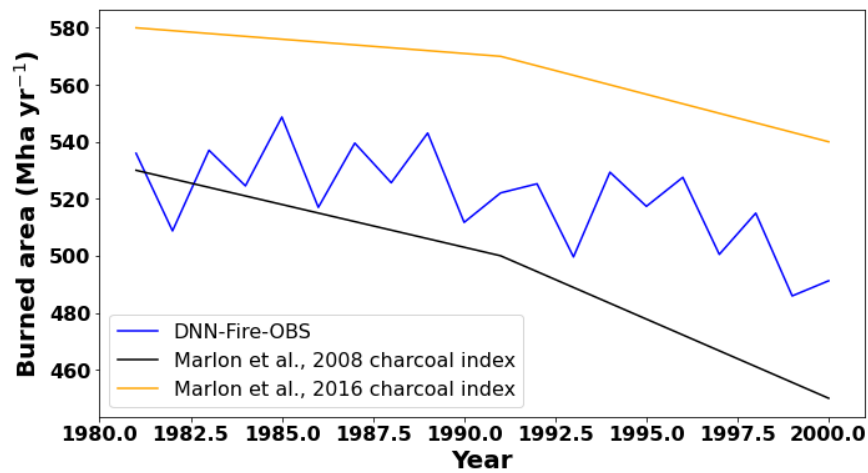


705

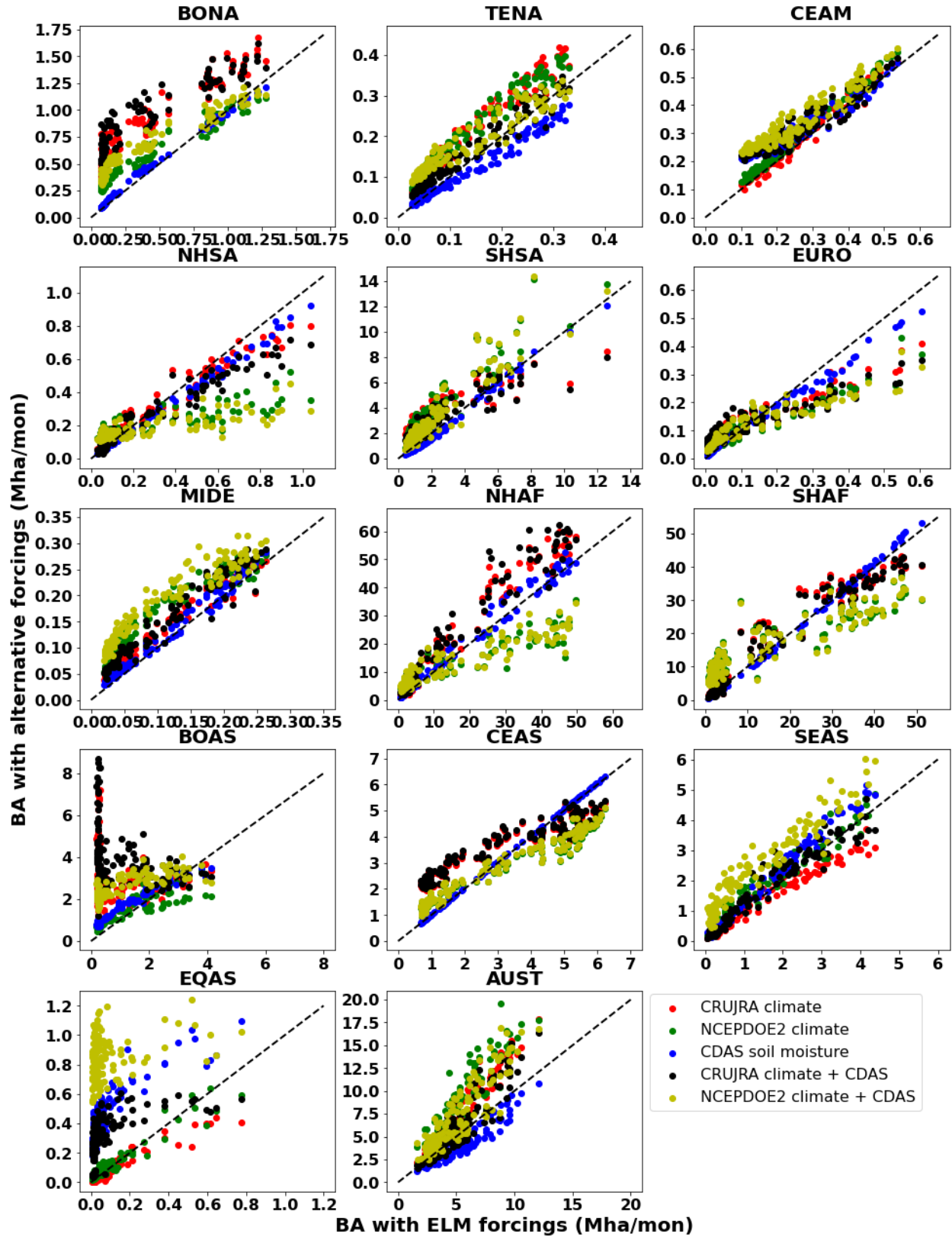
706 **Figure S2.** Performance of surrogate model (DNN-Fire) compared with ELMv1 process-based  
 707 model (BASE-Fire).  
 708



709 **Figure S3.** Seasonal cycles of fine-tuned Deep Neural Network wildfire model (DNN-Fire-OBS)  
 710 and observations over 14 GFED fire regions.  
 711  
 712  
 713



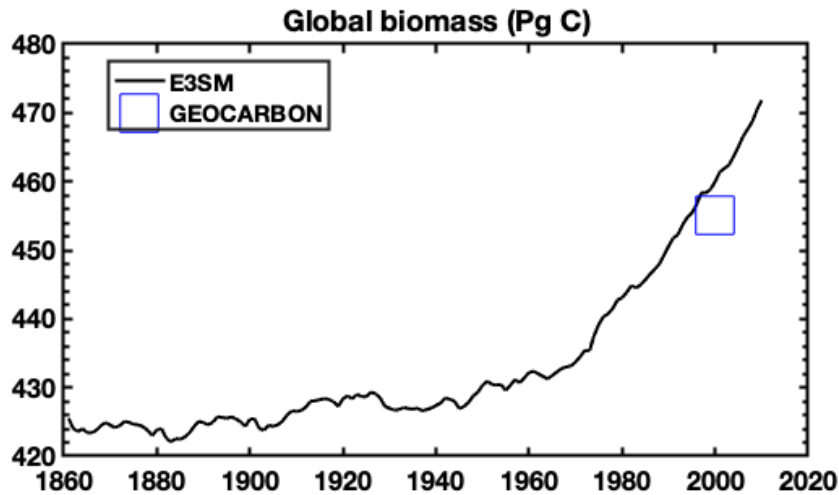
714 **Figure S4.** Comparison of DNN-Fire-OBS model simulated global burned area during 1981-  
 715 1999 with two charcoal index inferred burned area.  
 716



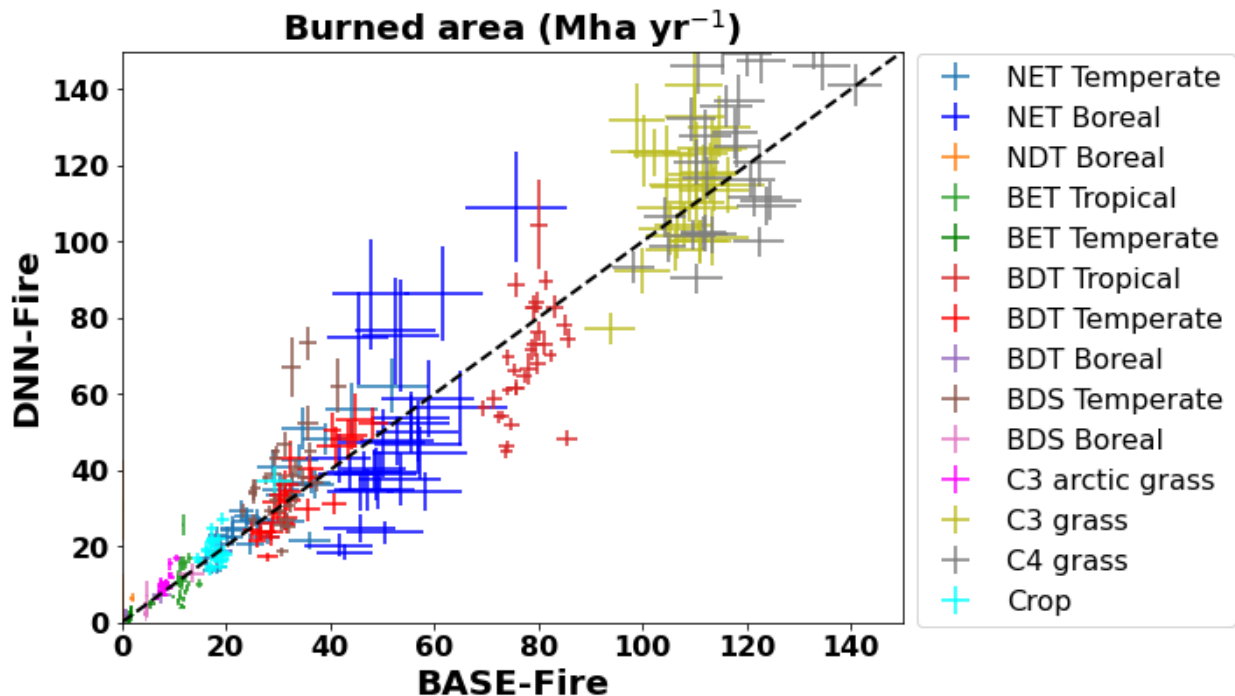
717  
718  
719

**Figure S5.** Sensitivity of modeled burned area (2001-2010 long-term averaged) to climate forcings (including temperature, precipitation, wind speed, relative humidity) and soil moisture.

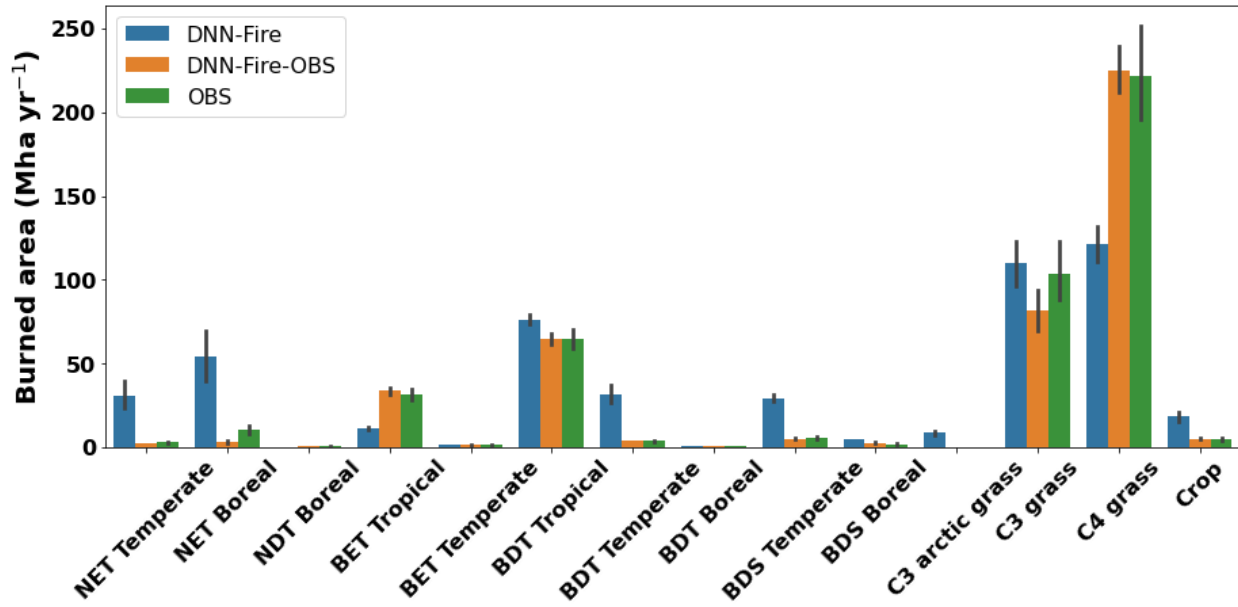
720 X-axis was burned area simulated by the default model using GSWP3 climate forcing and  
 721 ELMv1 simulated soil moisture. Y-axis were models with alternative climate forcing (CRUJRA,  
 722 NCEPDOE2) and soil moisture product (NCEP CDAS soil moisture).  
 723  
 724



725  
 726 **Figure S6.** 3SM simulated global vegetation biomass [425-472 PgC] and observational based  
 727 estimate of present-day living biomass (455 PgC GEOCARBON).  
 728



729  
 730 **Figure S7.** The performance of the Deep Neural Network wildfire model (DNN-Fire), compared  
 731 with the original ELMv1 process-based wildfire model (BASE-Fire) aggregated over 14 plant  
 732 functional types between years 2001 and 2010.  
 733  
 734



735  
736  
737  
738  
739

**Figure S8.** A comparison of wildfire burned area among Deep Neural Network wildfire model (DNN-Fire), Deep Neural Network wildfire model fine-tuned with observed burned area (DNN-Fire-OBS), and observations for 14 plant functional types.